



Synthesis of tungsten ditelluride thin films and highly crystalline nanobelts from pre-deposited reactants

John B. Mc Manus^{1,2} · Cansu Ilhan^{1,2} · Bastien Balsamo^{2,3} · Clive Downing^{1,2} · Conor P. Cullen^{1,2} ·
Tanja Stimpel-Lindner⁴ · Graeme Cunningham^{1,2} · Lisanne Peters^{1,2} · Lewys Jones^{2,5} · Daragh Mullarkey⁵ ·
Igor V. Shvets⁵ · Georg S. Duesberg^{1,4} · Niall McEvoy^{1,2}

Received: 23 April 2020 / Revised: 9 July 2020 / Accepted: 9 July 2020 / Published online: 9 September 2020
© The Nonferrous Metals Society of China 2020

Abstract

Tungsten ditelluride (WTe₂) is a layered transition metal dichalcogenide (TMD) that has attracted increasing research interest in recent years. WTe₂ has demonstrated large non-saturating magnetoresistance, potential for spintronic applications and promise as a type-II Weyl semimetal. The majority of works on WTe₂ have relied on mechanically exfoliated flakes from chemical vapour transport (CVT)-grown crystals for their investigations. While producing high-quality samples, this method is hindered by several disadvantages including long synthesis time, high-temperature annealing and an inherent lack of scalability. In this work, a synthesis method is demonstrated that allows the production of large-area polycrystalline films of WTe₂. This is achieved by the reaction of pre-deposited films of W and Te at a relatively low temperature of 550 °C. Sputter X-ray photoelectron spectroscopy reveals the rapid but self-limiting nature of the oxidation of these WTe₂ films in ambient conditions. The WTe₂ films are composed of areas of micrometre-sized nanobelts that can be isolated and offer potential as an alternative to CVT-grown samples. These nanobelts are highly crystalline with low defect densities indicated by transmission electron microscopy and show promising initial electrical results.

Keywords Two-dimensional materials · Tungsten ditelluride · Film conversion · Electrodeposition · Nanoelectronics

Electronic supplementary material The online version of this article (<https://doi.org/10.1007/s42864-020-00056-4>) contains supplementary material, which is available to authorized users.

✉ John B. Mc Manus
mcmanuj2@tcd.ie

✉ Niall McEvoy
nmcevoy@tcd.ie

¹ School of Chemistry, Trinity College Dublin,
Dublin 2 D02 PN40, Ireland

² AMBER Centre, CRANN Institute, Trinity College Dublin,
Dublin 2 D02 PN40, Ireland

³ SIGMA Clermont, Université Clermont Auvergne,
63000 Clermont-Ferrand, France

⁴ Institute of Physics, EIT 2, Faculty of Electrical Engineering
and Information Technology, Universität der Bundeswehr
München, 85579 Neubiberg, Germany

⁵ School of Physics, Trinity College Dublin,
Dublin 2 D02 PN40, Ireland

1 Introduction

Transition metal dichalcogenides (TMDs) are a family of layered materials whose nanoscale forms have been extensively studied over the last number of years. This interest is due to their varied and layer-dependent properties, which give them a wide range of potential applications [1, 2].

Unlike some of the more commonly studied TMDs, such as MoS₂ and WS₂ that exist predominantly in the trigonal prismatic 2H phase, WTe₂ is most stable in the distorted octahedral T_d phase, making it unique among the Group VI TMDs [3, 4]. This structure means WTe₂ is semimetallic and opens up unique electronic properties, such as topological electronic states [5]. Thorough investigations of the structure and electrical properties of bulk WTe₂ were carried out in the 1950s and 1960s, with particular emphasis placed on its thermoelectric properties [3, 6–11]. However, it is only recently that investigations have focused on mono- and few-layer forms.

WTe₂ can be considered a layered or two-dimensional (2D) material, though it does also have some

one-dimensional (1D) character due to its distorted octahedral structure. This distortion causes quasi-1D chains of W atoms to be formed within the layers, schematically shown in Fig. 1a insert [4]. This leads to a strong anisotropy in properties such as the conductivity and mechanical

response within the monolayer [12]. It also manifests in the tendency of WTe_2 crystals to grow anisotropically [13]. The crystals are generally longest along the b crystallographic direction, which is parallel to the 1D tungsten chains.

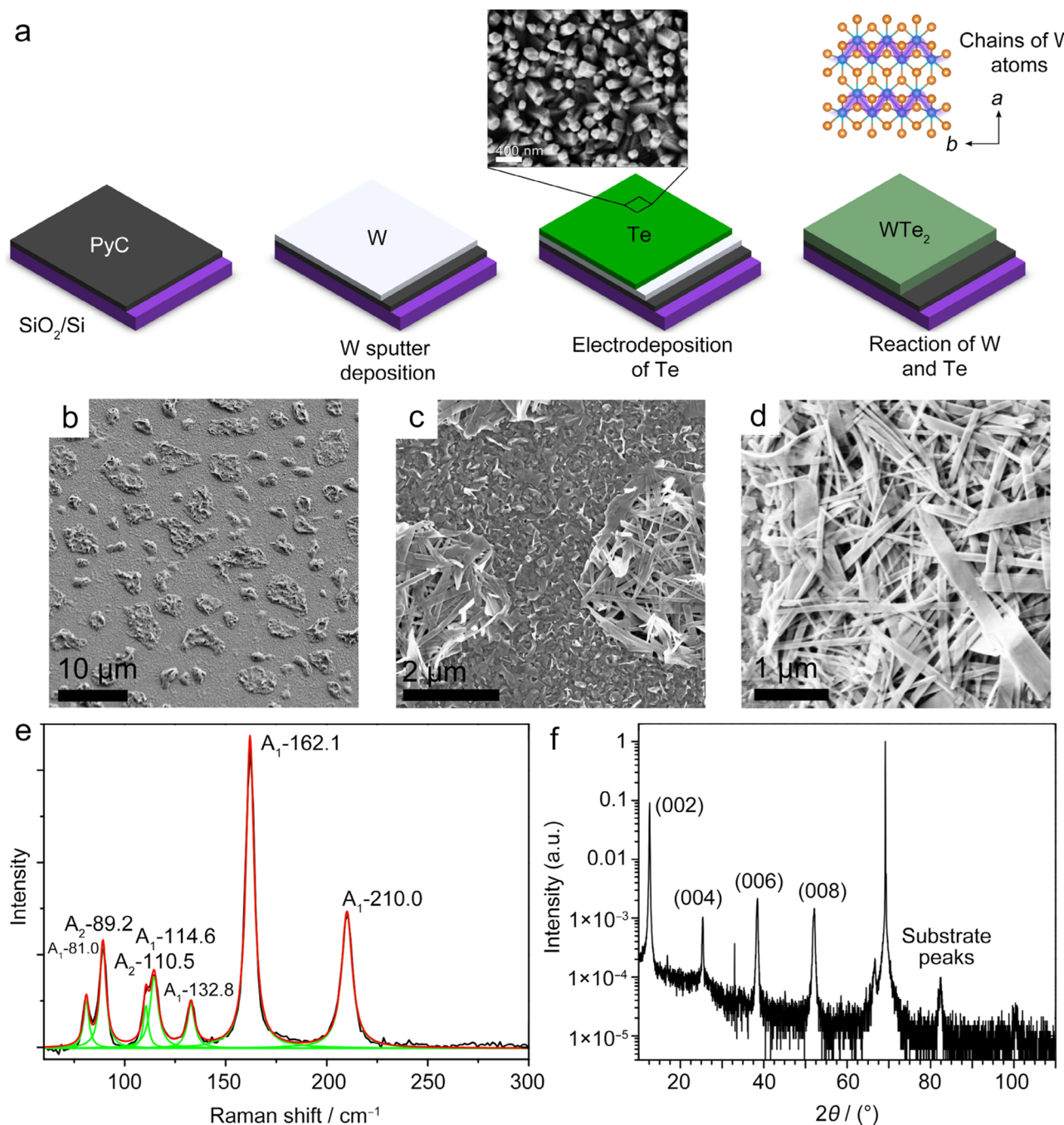


Fig. 1 **a** Process steps involved in WTe_2 film synthesis with an scanning electron microscopy (SEM) image of the surface of the Te film before conversion to WTe_2 . Inset: Diagram of the 1D W atom chains in the WTe_2 structure. **b–d** SEM images of the surface of WTe_2 film synthesised from the 20 nm initial W layer, 20,000 pulse deposition of Te and annealed at 550 °C. **e** Raman spectrum of the same film

showing the expected modes of bulk-like WTe_2 . Modes are fitted with Lorentzian peaks to extract positions. **f** X-ray diffraction (XRD) pattern of WTe_2 film, synthesised from the 20 nm initial W layer, showing the (002) and associated reflections. A number of substrate peaks are also visible above 60°

Applications-centred studies of WTe_2 have historically focused on thermoelectrics but more recent studies have examined a much broader range of potentially interesting properties and applications. Experimental investigations of the electronic properties of WTe_2 have demonstrated large, non-saturating magnetoresistance and high charge-carrier mobilities of up to $10,000 \text{ cm}^2 \cdot \text{V}^{-1} \cdot \text{s}^{-1}$ [14–16]. There are also reports of ferroelectricity [17] and superconductivity [18, 19] in WTe_2 . Furthermore, it was the first material to be suggested as a potential type-II Weyl semimetal [20]. Since this prediction, there has been a number of experimental reports that have lent credence to this assertion [21, 22].

Other works have examined WTe_2 for use in applications such as nanoscale electrical interconnects [23], electrocatalysis [24, 25] and as an anode material for Na-ion batteries [26]. Additionally, WTe_2 has been touted as a promising candidate for large-gap quantum spin Hall insulators [5, 21, 22]. Lastly, through electrochemical investigations, the possibility of using WTe_2 as a catalyst for the hydrogen evolution reaction (HER) has been examined [24, 27–30].

The majority of reports, especially those examining its electronic properties, have focused on mechanically exfoliated flakes from chemical vapour transport (CVT)-grown crystals of WTe_2 [14–16, 31–33]. While CVT does produce exceptionally high-quality crystals, it is a time- and energy-intensive process requiring long anneals at temperatures of up to $1000 \text{ }^\circ\text{C}$. The subsequent laborious mechanical exfoliation and transfer process also limit the scalability of any devices made using this method.

There has been some work on the bottom-up growth of nanoscale WTe_2 ; however, large-area and reproducible synthesis remains an open challenge [34, 35]. Table 1 gives an overview of a range of publications that synthesised WTe_2 on the nanoscale. Chemical vapour deposition (CVD) growth of WTe_2 has achieved single-crystal monolayers with lateral dimensions on the order of tens to hundreds of micrometres from Te, WO_3 and WCl_6 precursors [34, 35, 40]. Despite requiring high growth temperatures, $650\text{--}800 \text{ }^\circ\text{C}$, CVD growth remains the most promising method for high-quality monolayer synthesis. Nevertheless, there remains significant challenges to overcome before large-area, reproducible and layer-controlled growth of WTe_2 is achieved.

Large-area growth of polycrystalline films of WTe_2 has been achieved, with thicknesses ranging from a few to tens of monolayers [41, 43, 46, 47]. These films are generally synthesised by the conversion of a pre-deposited W source on a substrate. This is accomplished by exposure of the W source to Te vapour in a controlled atmosphere at an elevated temperature. These methods offer the advantage of producing large-area films in a scalable manner. The final thickness of the film can also be determined by the thickness of the initially deposited W source. These polycrystalline films have grain sizes ranging from less than 10 nm to $\sim 100 \text{ nm}$.

This means that while promising for a range of applications, these films are not suitable for many electronic applications due to high and variable levels of unintentional doping and high densities of scattering centres [54].

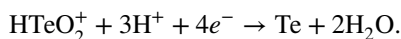
A number of other works have synthesised WTe_2 on the nanoscale using methods such as solution-based growth and molecular beam epitaxy (MBE) [26, 48, 53]. The work on beam-interrupted MBE synthesis of WTe_2 demonstrates the growth of large-area and high-quality films with a high degree of thickness control, making it a promising choice for synthesis of WTe_2 . However, there are a number of challenges associated with this synthesis that limit its applicability, such as the necessity for high vacuum, large Te excess and careful substrate selection.

This discussion shows that while substantial progress has been made in the synthesis of nanoscale WTe_2 , the field is far from mature. The majority of works relying on CVT means that there is a pressing need for further work on alternative, lower-temperature synthesis methods, especially those which are scalable.

In this work, we present a method to synthesise polycrystalline films consisting of WTe_2 nanobelts, with individual nanobelts of up to $10 \text{ }\mu\text{m}$ in length. These are synthesised by annealing pre-deposited films of W and Te at a relatively low temperature of $550 \text{ }^\circ\text{C}$. Characterisation of the films reveals that their surface is prone to oxidation but this is self-limiting and does not extend into the bulk. Due to their large lateral size, these micrometre-scale and single-crystal nanobelts of WTe_2 can be isolated and characterised individually. The high crystallinity of the nanobelts implies their suitability for applications previously demonstrated using CVT-grown flakes. To show this, individual nanobelts were electrically characterised. The ability to access both large-area films and single-crystalline flakes demonstrates the versatility of this method to produce high-quality samples of WTe_2 in an efficient manner.

2 Experimental

A film of W was deposited onto the substrate using a Gatan PECS Ar-ion sputtering tool. A layer of Te was subsequently deposited on top of this by electrodeposition. Te was reduced from solution, $0.02 \text{ mol} \cdot \text{L}^{-1} \text{ TeO}_2$ in $1 \text{ mol} \cdot \text{L}^{-1}$ nitric acid, in an electrochemical cell. A platinum counter electrode and a Ag/AgCl reference electrode were used. This is shown in Fig. S1. The reduction proceeded via the reaction [55]:



A pulsing sequence was used during the deposition, which consisted of 10 ms pulses of -0.3 V applied to the working electrode with respect to the reference electrode

Table 1 Literature review of published synthesis techniques to produce nanoscale WTe₂

Method description	Subsequent processing to obtain 2D form	Material characteristics	Synthesis T (°C)	Growth time	Ref
CVT	Mechanical exfoliation (ME)	Single-crystal flakes	750	11 days	[14]
CVT	ME	Single-crystal flakes	800	10 days	[36]
CVT	ME	Single-crystal flakes	900	4 days	[31]
CVT	ME	Single-crystal flakes	1000	8 days	[37]
CVT	ME	Single-crystal flakes	800	11 days	[22]
CVT	ME	Single-crystal flakes	1020	5 days	[38]
CVT	ME	Single-crystal flakes	950	3 days	[39]
CVT	ME	Single-crystal flakes	1100	4 days	[32]
CVD, ammonium tungstate hydrate and KCl promoter	None	Monolayer flakes, length ~ 350 μm	800	20 min	[34]
CVD, WCL ₆ /WO ₃ precursor	None	Monolayer flakes, length ~ 350 μm	820	20 min	[40]
CVD WCl ₆ precursor	None	Polycrystalline film; thickness of above 5 nm	500	20 min	[41]
CVD, ammonium metatungstate precursor	None	Monolayer flakes, length ~ 50 μm	650	6 min	[35]
CVD, WO ₃ precursor and KI growth promoter	None	Monolayer flakes, length 10 s of μm	700	1 h	[42]
Film conversion, pre-deposited W/WO ₃	None	Large-area polycrystalline film, thickness of 6 nm, grain size of ~ 6 nm	650	60 min	[43]
Film conversion, pre-deposited WO ₃ nanowires	None	Nanowires	500	10 min	[44]
Film conversion, pre-deposited W, close proximity Ni _x Te _y source	None	Large-area polycrystalline films, thickness of few layers to bulk, grain size of tens of nm	500	10–30 min	[45]
Film conversion, pre-deposited W, need H ₂ present during reaction	None	Large-area polycrystalline film, thickness ≥ 1 nm, grain size of tens of nm	800	50 min	[46]
Film conversion, pre-deposited W and Cu	None/ Mechanical transfer	Large-area polycrystalline film of WTe ₂ nanobelts	500	10 min	[47]
MBE, highly oriented pyrolytic graphite (HOPG)/MoS ₂ substrates	None	Large-area films	275	1.5 nm·h ⁻¹	[48]
CVT	Sonication	Quantum dots	N/A	N/A	[49]
Pulsed laser deposition	None	Polycrystalline film; thickness of ≥ 5 nm	N/A	N/A	[50]
Pulsed laser deposition	Post-deposition anneal with Te	Highly crystalline, thickness of ~ 100 nm	700	1 nm·min ⁻¹ growth rate, 48 h anneal	[51]
Solution-phase growth	None	Nanostars	320	24 h	[25]
Solution-phase growth	None	Nanostructures, ~ 200 nm	260	~ 2 h	[52]
Solution-phase film formation, WCl ₄ precursor	Microwave heating	Large-area polycrystalline film, few-layer thickness, grain size of 6 nm	Unspecified	Unspecified	[53]

N/A: Not applicable

with 50-ms gaps between these. Varying the number of pulses in a deposition served to control the quantity of Te deposited on the sample. Using a pulsing potential was found to yield a more uniformly deposited film of Te [55]. Further detail is given in a previous work using a similar method to synthesise MoTe_2 [56].

The substrates used throughout the work are pyrolytic carbon (PyC) on a 300-nm thermal SiO_2 on Si wafer. The PyC layer is not necessary but served to improved conductivity during the electrodeposition. The PyC was grown by CVD of acetylene at 950 °C for 30 min on SiO_2/Si substrates in a hot-wall and quartz-tube furnace [57].

Following the Te deposition, the films were converted to WTe_2 in an ATV PEO 604 quartz furnace under a nitrogen atmosphere at a pressure of ~ 700 mbar ($\sim 70,000$ Pa). The growth temperature was typically 550 °C but other growth temperatures were also investigated. Nested crucibles were used to maintain a high partial pressure of Te in the vicinity of the samples while avoiding contaminating the furnace with high quantities of Te, as shown in Fig. S1b. The temperature was ramped at $180\text{ }^\circ\text{C}\cdot\text{min}^{-1}$ and held at the growth temperature for 90 min. The samples were then allowed to cool to near room temperature ($< 30\text{ }^\circ\text{C}$) under N_2 over a period of ~ 3 h before removal from the furnace. During the cooling, at $\sim 320\text{ }^\circ\text{C}$, the pressure was lowered from ~ 700 mbar ($\sim 70,000$ Pa) to 13 mbar (1300 Pa) to ensure removal of any remaining Te. All samples are named by referring to the thickness of the starting W film.

Nanobelts of WTe_2 were mechanically transferred from the growth substrate using adhesive Nitto Denka BT-150E-CM tape. A schematic of this process is shown in Fig. S2. To grow the films with the largest possible WTe_2 nanobelts, samples with 40 nm of W and 40,000 pulses of Te were used.

SEM images were obtained with a Karl Zeiss Supra microscope operating at 3-kV accelerating voltage, 30- μm aperture and a working distance of ~ 3 –4 mm. The XRD measurement was performed on a Bruker D8 Discover with a monochromated Cu $\text{K}\alpha$ source.

A WITec Alpha 300R with a 532-nm excitation laser, with a power of $\sim 200\text{ }\mu\text{W}$, was used to collect the Raman spectra shown herein. All Raman measurements were taken using a spectral grating with 1800 lines/mm and a $100\times$ objective lens. Raman spectra shown are averages of maps which were generated by taking scans every 400 nm in the x and y directions, typically over an area of $20\times 20\text{ }\mu\text{m}$, making each spectrum an average of ~ 2500 spectra.

X-ray photoelectron spectroscopy (XPS) spectra were taken with a PHI VersaProbe III instrument equipped with a micro-focused, monochromatic Al $\text{K}\alpha$ source (1486.6 eV) and a dual-beam charge neutralisation used. Core-level spectra were recorded with a spot size of 100 μm and a pass

energy of 69 eV using PHI SmartSoft VersaProbe software, and processed with PHI MultiPak 9.8. Sputter XPS depth profiling was conducted using 1-keV Ar ions. Binding energies were referenced to the adventitious carbon signal at 284.8 eV. Spectral components were fitted using a Shirley background subtraction and appropriate line shapes. Relative atomic percentages were calculated using the relative sensitivity factors provided by the software CasaXPS.

Atomic force microscopy (AFM) was carried out on a Bruker Multimode 8 in ScanAsyst Air mode using Nanosensor PointProbe Plus tips. High-resolution transmission electron microscopy (HRTEM) analysis was performed in an FEI Titan transmission electron microscopy (TEM) at an acceleration voltage of 300 kV. Atomic-resolution scanning transmission electron microscopy (STEM) images were obtained with a Nion UltraSTEM200, using an HAADF detector, operated at 200 kV.

An overview of how STEM averaging was performed is that, initially, a small area of the sample (4 nm \times 4 nm in this case) with atomic resolution is chosen. The software then scans the remainder of the image and finds all the areas with which this image matches to a high degree. All of these areas (300 in this analysis) are then extracted and stacked to form an average image [58]. Further image processing then removes any distortion in the image [59].

For electrical measurements, samples were patterned by electron-beam lithography (EBL) before Ti/Au (5 nm/100 nm) contacts were deposited using electron-beam evaporation.

3 Results and discussion

3.1 Synthesis of WTe_2 films

Films of WTe_2 were synthesised by depositing a layer of W onto a target substrate using Ar-ion sputtering, followed by the electrodeposition of Te on top of this, as shown in Fig. 1a. The thickness and pattern of the W layer were defined during the sputtering process, while the electrodeposition allowed Te to be deposited in a controlled and directed manner onto each sample. This method gave local and well-defined quantities of both reactants directly on the sample. This avoided the need for a remote Te source and the challenges associated with this, such as requiring a high excess of reactant.

The layers of W and Te were then placed inside nested crucibles and loaded into a quartz furnace, where they were heated to form WTe_2 (Fig. S1b). The conversion typically took place at a dwell temperature of 550 °C for a period of 90 min under an inert atmosphere.

All samples are named based on their starting W thickness, as measured by the deposition tool's quartz crystal

monitor (QCM). The sample substrates were SiO₂/Si wafers with a ~300-nm layer of PyC to improve the uniformity of the Te film deposition [56]. The samples studied were ~1 cm × 1 cm in area but the process could be scaled up to produce larger area samples.

This synthesis method allowed the growth of large-area polycrystalline films of WTe₂. Figure 1b–d shows SEM images of a typical WTe₂ film synthesised from an initial 20 nm W layer. It is immediately apparent that the surface of the film consists of two differing morphologies. There are discrete patches, with dimensions of up to tens of micrometres, containing elongated WTe₂ nanobelts. The nanobelts are several micrometres in length and have widths of tens to hundreds of nanometres. Surrounding the patches of nanobelts are areas of smaller grains with lengths below 500 nm. The growth of elongated nanobelts is due to the quasi-1D nature of WTe₂, and similar growth of elongated WTe₂ flakes has been seen in a number of studies on CVD growth of WTe₂ [26, 34, 60]. The 1D chains of W in the lattice would be expected to be parallel to the long axis of the nanobelts.

The WTe₂ films are synthesised in a straight-forward and scalable manner with full coverage over the entirety of the sample. This compares favourably with the majority of previously reported growth methods for WTe₂ which are by-and-large laborious, time consuming and not scalable. Furthermore, the properties of the films—thickness and grain size—can be tailored by changing the parameters of the initial W and Te depositions.

Compared to typical film conversion methods, which have grain sizes of tens of nanometres, this work allows the growth of films made up of much larger crystals, on the order of micrometres. This is likely due to the growth occurring at a solid–liquid interface, rather than the typical solid–vapour one. Having the liquid Te in direct contact with the W layer counteracts the low activity of Te and facilitates the synthesis of WTe₂ at the comparatively low synthesis temperature and short time, which is similar to other works using Ni_xTe_y alloys [45]. Furthermore, H₂ is not required, unlike previously reported methods [46].

The morphology of these WTe₂ films is also influenced by the material properties—MoTe₂ and PtTe₂ previously grown using this method were found to have significantly different morphologies, with neither showing films consisting of large nanobelts [56, 61]

Raman analysis, shown in Fig. 1e, provides confirmation of the formation of WTe₂. This spectrum closely matches previously published spectra of bulk-like WTe₂, indicating the successful growth of T_d phase WTe₂ using this method [62–64]. The peaks at 81.0 cm⁻¹, 89.2 cm⁻¹, 114.6 cm⁻¹, 132.8 cm⁻¹, 162.1 cm⁻¹ and 210.0 cm⁻¹ are assigned the symmetry A₁, while the peak at 110.5 cm⁻¹ is A₂ [31, 65].

The Raman spectrum does not indicate any modes associated with oxides or other contaminants in the films.

Confirmation of the presence of WTe₂ throughout the surface was provided by Raman spectroscopy mapping (Fig. S3). While there are two morphologies present on the surface, which look quite different under optical microscopy and SEM, Raman spectroscopy mapping confirms that they are both T_d WTe₂.

XRD further confirmed the conversion of the W and Te films to WTe₂. XRD results are shown in Fig. 1f, and the diffraction pattern measured is consistent with previously reported XRD of WTe₂ with the (002), (004), (006) and (008) peaks being most prominent [3]. As the film is polycrystalline, there is a significant background and noise in the diffraction pattern. This made it infeasible to perform further analysis, such as extracting average grain size.

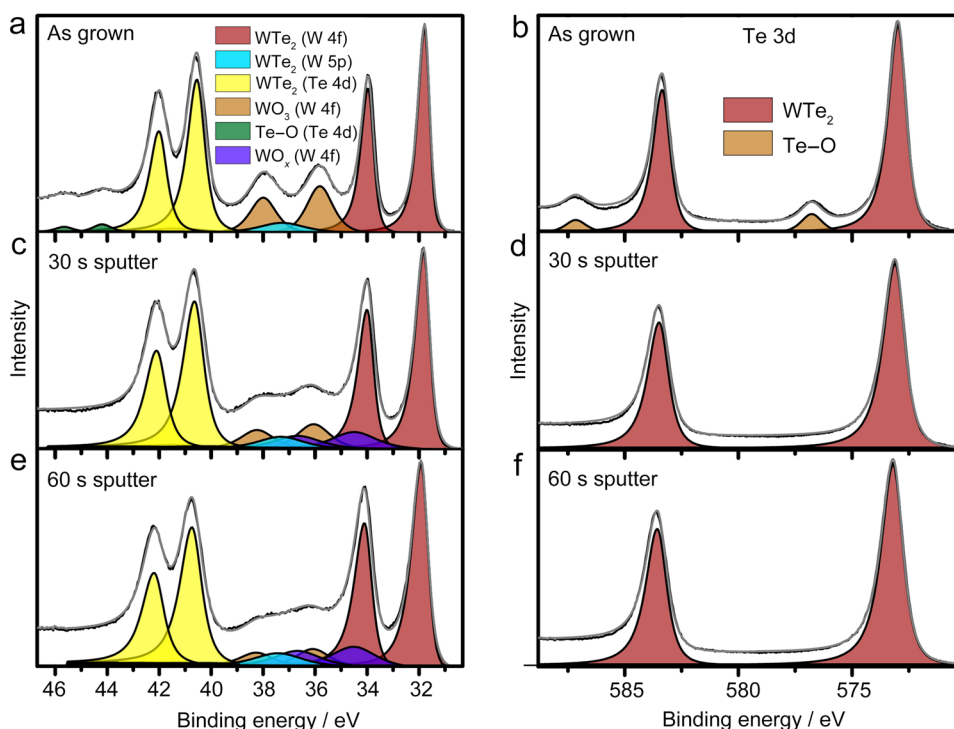
To obtain more quantitative and stoichiometric information, the films were analysed using XPS. This also gave information on the stability of the films, which can be considered important as previous reports have indicated a strong tendency for WTe₂ to oxidise in ambient conditions [35, 39, 66].

The XPS results are shown in Fig. 2. Shown in Fig. 2a is the W 4f core-level region of WTe₂, the W 5p and Te 4d core levels are also visible in this energy window; however, the analysis here only focuses on the W 4f core levels, as these are the most intense. There are two doublets present for the W 4f core level, one associated with WTe₂ and the other with WO₃. 30% of the W atoms are in the form of WO₃, with the remaining 70% in WTe₂. Similarly, in Fig. 2b, there are two doublets associated with the Te 3d core level, one corresponding to Te bound to W as WTe₂ and the other for Te in the form of oxides. Te on the surface is predominantly in the form of WTe₂, with only 8% of the atoms bound to oxygen. The stoichiometry of WTe₂ on the surface was found to be WTe_{1.8}, indicating a slight deficiency in Te. Finally, the asymmetric nature of the WTe₂ peaks indicates the (semi-) metallic nature of the sample.

3.2 Oxidation of WTe₂ films

The level of oxidation observed on the surface of the WTe₂ film implies that it is prone to degradation in atmosphere, more so than other telluride TMDs such as MoTe₂ and PtTe₂ that have shown low oxidation levels when similarly analysed [56, 61]. Previous works on the susceptibility of WTe₂ to oxidation have concluded that the oxidation of the first few atomic layers of WTe₂ is extremely rapid; however the oxidation is self-limiting and tends not to extend far into the bulk [35, 39, 66, 67]. Isolating WTe₂ from oxygen and water, either through storage in an inert atmosphere or encapsulation, serves to greatly inhibit the oxidation [67].

Fig. 2 **a, c, e** XPS spectra of the W 4f region for a WTe₂ sample as grown, after 30 s of sputtering and after 60 s of sputtering, respectively. **b, d, f** Same data for the Te 3d binding energy region of the WTe₂ sample. The sample was synthesised at 550 °C from an initial 20 nm W film with a 20,000 pulse Te deposition



It is the surface layer (less than 10 nm) that is exclusively probed by XPS, potentially leading to an over estimation of the over-all oxidation level of the sample. To offer further understanding of this, the sample was analysed using sputter XPS.

Sputter XPS involves repeated cycles of *in situ* sputtering and XPS analysis, allowing the elemental composition both at the surface and at various depths in the bulk of the sample to be measured. The sputter XPS process is described in more detail in the methods section.

Two rounds of 30-s Ar sputtering were carried out, with the results shown in Fig. 2c–f. The Te 3d core-level spectra show that after 30 s of sputtering only a single doublet corresponding to Te in the form of WTe₂ is visible. The signal of Te bound to oxygen is below the detection limit of the tool, indicating that the Te oxide is only present on the surface with virtually none in the bulk of the sample.

The signal from WO₃ reduces significantly after sputtering, from about 30% initially, to 10% after 60 s. During the same time, the percentage of W atoms in the form of WTe₂ remains roughly constant at 70%. The difference is accounted for by the development of a WO_x signal that accounts for slightly less than 20% of W atoms after 60 s of sputtering. This WO_x peak is not present in the surface scan but develops after sputtering. All the W peaks broaden after sputtering, due to damage or amorphisation caused by the sputtering process.

The sputtering XPS shows that TeO₂ and WO₃ are primarily present on the surface of the films. However, a WO_x signal is present after sputtering, and the percentage of W atoms present as either WO₃ or WO_x is roughly constant throughout. Furthermore, the overall ratio of W to Te on the surface changes after sputtering, with the sample becoming increasingly deficient in Te. The proposed explanation of these observations is that Te is preferentially sputtered, meaning that the sample becomes more W rich during this process, and WO₃ is not effectively sputtered but rather becoming a substoichiometric WO_x [68]. This also correlates with previous reports that indicate the self-limiting nature of WTe₂ oxidation. Furthermore, this conclusion also aligns with why no strong oxide signal is observed in the Raman spectroscopy—Raman is much less surface sensitive than XPS so the WTe₂ signal remains dominant.

3.3 WTe₂ growth mechanism

The majority of films in this work was synthesised at a temperature of 550 °C; however, WTe₂ was successfully grown over a range of temperatures. Figure 3a shows Raman spectra of films synthesised at a range of temperatures. At 350 °C, the only Raman peaks visible are attributed to elemental Te [69]. For all growth temperatures between 450 °C and 650 °C, characteristic peaks associated with bulk-like WTe₂ are observed. No discernible peaks are visible in the

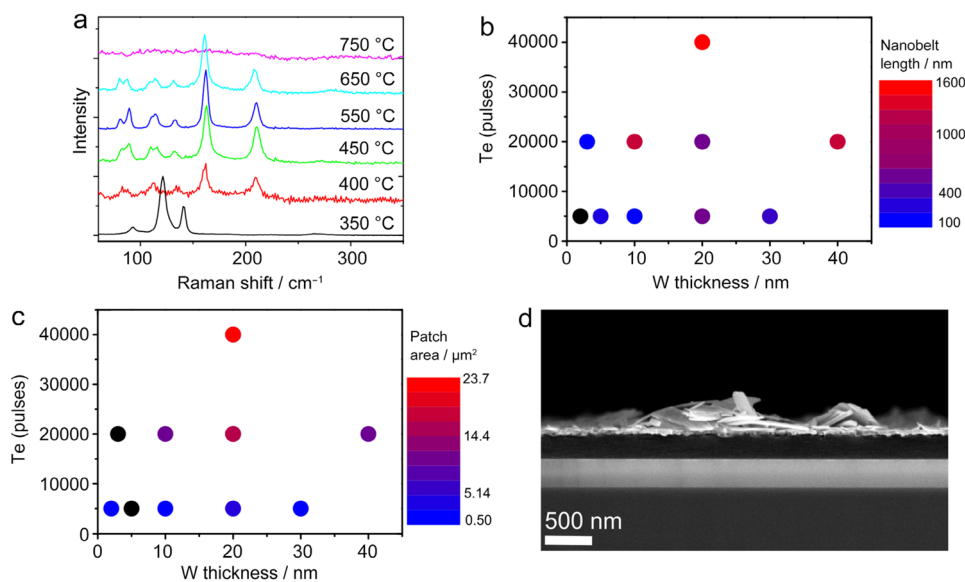


Fig. 3 **a** Raman spectra of WTe₂ films synthesised at a range of temperatures between 350 and 750 °C. At 350 °C only the signal for Te is present, and between 450 and 650 °C there is a strong signal corresponding to bulk-like WTe₂. At 400 °C there is a weak WTe₂ signal and at 750 °C there are no discernible Raman peaks. **b** Plot of the variation of average nanobelt length (100–1600 nm) with changes in the amount of W and Te present. The thickness of the initial layer

of W was varied between 2 and 40 nm. Between 5000 and 40,000, pulses of Te were electrodeposited on the surface. Red indicates long nanobelts. **c** Variation of patch area with changes to W and Te amounts, displayed in a similar manner to plot **b**. **d** Cross-section SEM image of a cleaved substrate and WTe₂ film showing raised patches of WTe₂ nanobelts. The film was synthesised at 550 °C from an initial 20 nm W film with a 20,000 pulse Te deposition

750 °C scan indicating that no WTe₂ or Te is present following growth at this temperature.

Some understanding of the influence of growth temperature can be achieved by examining the binary phase diagram for W–Te (Fig. S4). As the sample reaches the Te melting point—450 °C—a liquid WTe_x alloy forms at the boundary between the W and Te, as a result of W dissolving into the liquid Te. It is clear from the phase diagram, that in this temperature range (450 °C–650 °C), the alloy remains liquid for only a very small percentage W, beyond which it becomes supersaturated. This means that, as more W dissolves into Te, solid WTe₂ crystals begin to nucleate and grow within the liquid alloy. Concurrent with this Te evaporates, further driving the growth of WTe₂ crystals. If the growth time is sufficiently long, all unreacted Te evaporates, leaving a film solely consisting of WTe₂ during the cool-down. Below 450 °C, the formation of an intermixed layer is greatly reduced due to Te not melting, dramatically hindering the growth, as shown by the poor WTe₂ Raman signal at 400 °C and the absence of any discernible WTe₂ Raman signal at 350 °C.

The upper bound of ~650 °C cannot be understood from the phase diagram, which indicates stability of WTe₂ up to ~1000 °C. The proposed reason for the upper bound seen here is that Te evaporates too quickly to react effectively, or any WTe₂ that does form decomposes through loss of Te due to the Te-deficient environment [71, 72]. This loss would not

occur in CVT growth systems due to the vessel being sealed, maintaining high Te concentrations throughout the growth, and allowing the use of higher growth temperatures.

By changing the initial quantity of W and Te on the samples, it was possible to control the thickness of the films and also the average sizes of the WTe₂ grains/nanobelts. The average nanobelt size was primarily determined by the quantity of Te present, except for the thinnest films where both the W and Te quantity were important, as shown in Fig. 3b. This figure shows W and Te quantities on the x- and y-axes, respectively, with the average nanobelt size indicated by the colour of the data points. The lesser effect of W suggests that below a certain point, it limits the growth, but above a particular threshold, it no longer has a strong influence on the nanobelt size. The average length of the nanobelts could be varied between < 100 nm and 1600 nm over the parameter space examined.

The size of the WTe₂ crystals grown in the film is affected by the Te quantity in two ways. First, more Te provides more reactant in general, allowing larger crystal growth. Second, since the reaction to form WTe₂ occurs in the liquid Te alloy, more Te provides a greater duration for the reaction to occur before Te vaporises.

The two distinct morphologies on the surface can be similarly explained. During growth, Te dewets and forms droplets on the surface. These droplets serve as areas of high local reactant quantity and long growth times,

enabling much larger crystals to grow than in surrounding areas. Furthermore, the area of these patches containing larger WTe_2 nanobelts also increases with increasing Te quantity, as shown in Fig. 3c.

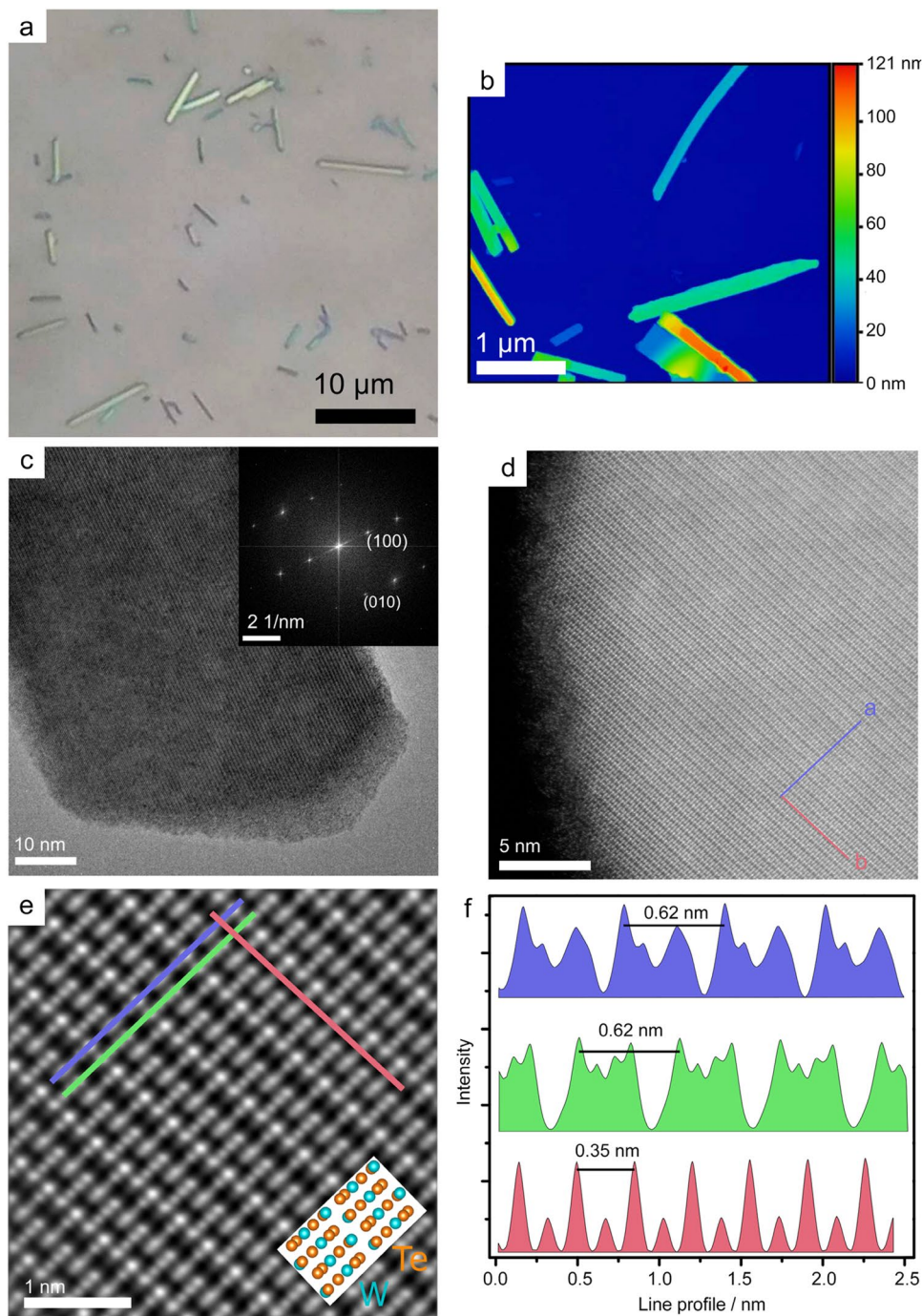
These results correlate well with the previously published reports for a similar system in the work of Kwak et al. [47]. However, a notable difference is that if one looks at a cross-section SEM of the films in this work, shown in Fig. 3d, it is clear that the droplets were raised above the majority of the surface and that the WTe_2

crystals grew within them. This suggests that W tends to dissolve into Te rather than Te etching down into the W, as proposed in the previous work [47].

3.4 Characterising individual nanobelts

The majority of film conversion growth methods result in polycrystalline films with grain sizes between 10 and 100 nm. In contrast, the films produced in this work can be optimised to have nanobelts with lengths of up to 10 μm .

Fig. 4 **a** Optical image of transferred WTe_2 nanobelts. These were transferred from WTe_2 synthesised from 20 nm W and 40,000 pulses of Te deposition. **b** AFM image of same sample. **c** HRTEM image of a WTe_2 nanobelt. Insert: FFT of image **c**. **d** ADF-STEM image of the edge of a WTe_2 nanobelt, with the WTe_2 crystallographic directions marked. **e** Atomic-resolution ADF image of WTe_2 crystal, compiled by averaging areas of **d**. Insert: atomic positions of WTe_2 for appropriate crystallographic direction. **f** Profiles of intensity measured from lines indicated in **e**



The larger crystal size, discrete and separate nature of the nanobelts allowed us to develop a method to isolate individual WTe_2 nanobelts for further study by transferring them onto another substrate. This allowed examination of individual nanobelts in a manner not possible for a film. Details of this transfer method are given in Fig. S2.

Figure 4a and b show optical and AFM images of the nanobelts on the destination substrate. The largest nanobelt measures about 10 μm long, width of ~ 600 nm and thicknesses of ~ 130 nm. While flakes with smaller lateral sizes were correspondingly thinner (10–20 nm), all nanobelts examined are nevertheless well into the range of displaying bulk-like characteristics.

The transfer of individual WTe_2 nanobelts made it possible to examine them using TEM. Initial analysis of the nanobelts was carried out using HRTEM. Figure 4c is an HRTEM image of a nanobelt, with the corresponding fast Fourier transform (FFT) shown in the insert. These highlight the crystalline nature of WTe_2 with clear lattice fringes visible in the TEM image and discrete spots in the FFT.

To further examine the crystal structure and quality, annular dark-field scanning TEM (ADF-STEM) was carried out on the nanobelts. This analysis allowed atomic-resolution images to be captured, shown in Fig. 4d. This image clearly shows that these nanobelts have a high level of crystallinity, with no grain boundaries visible over the area examined.

STEM images were taken from either end of a WTe_2 nanobelt, several micrometres in length, and the FFTs of these images are shown in Fig. S5. These match to a very close degree, offering further confirmation of the single-crystalline nature of the nanobelts. It should be noted that there is some distortion in the images shown here. The

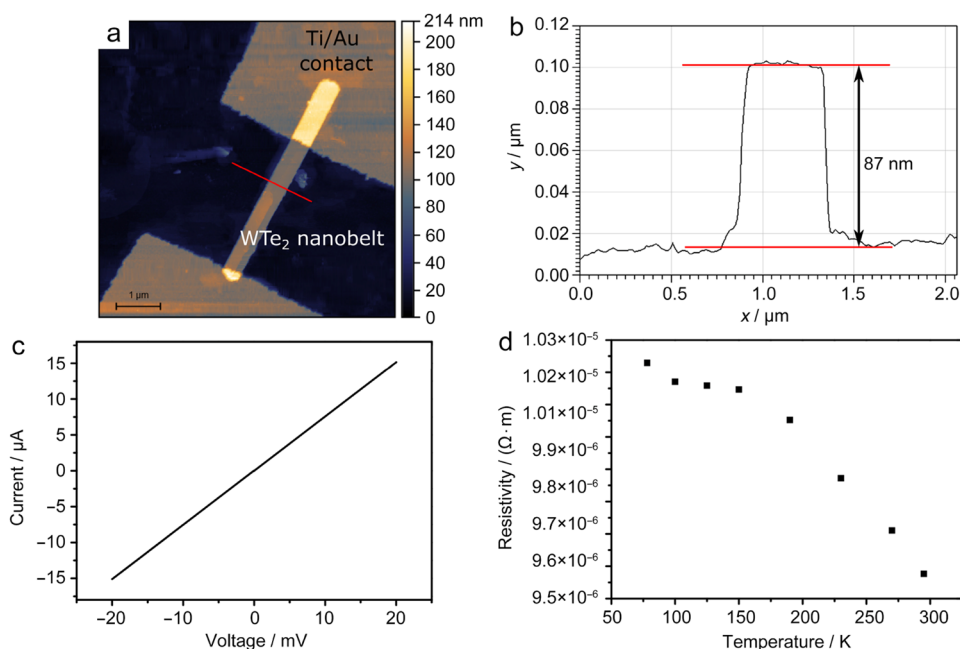
orthogonal crystalline directions have measured angles of $\sim 87^\circ$ between them. This is thought to be most likely due to small stage drift or slight misalignment of the crystalline axis during imaging [73].

The STEM analysis indicates the highly crystalline nature of the nanobelts, without significant defect densities visible. As there are no visible grain boundaries within the nanobelts, they are potentially comparable to mechanically exfoliated flakes from CVT-grown crystals. This could open up a much quicker and lower-temperature synthesis route to produce micrometre size WTe_2 flakes for a range of studies.

By applying a spatial averaging and scan-distortion correction technique to Fig. 4d, the image shown in Fig. 4e was obtained [59]. This averaging technique was discussed previously in the methods section [58]. This shows very clear atomic resolution giving the expected T_d structure of WTe_2 . This matches well to the previously published analysis of WTe_2 [4, 47].

Measuring the intensity along the two crystallographic directions of this image gave the line profiles shown in Fig. 4f [74]. The red profile shows a repeating pattern every 0.35 nm. This matches closely to the lattice constant of WTe_2 along the [010] crystallographic direction of 0.3496 nm. While the repeat period in the orthogonal direction of 0.62 nm is very close to the unit cell length of 0.6282 nm for WTe_2 along the [100] direction. Using this information, along with the spacings obtained from the FFTs, allowed the conclusion to be drawn that it is the (001) lattice planes that are examined in this case. A model of the expected atomic positions is shown in the inset of Fig. 4e. This matches quite well to the alternating lines of atoms observed in the STEM image. When viewed from

Fig. 5 **a** AFM image of the contacted WTe_2 nanobelt device. **b** Height profile of the nanobelt along the line marked in **a**. **c** Two-terminal current–voltage (IV) measurement of the WTe_2 nanobelt device. **d** Plot showing the change in resistivity of the nanobelt as the temperature is increased from 78 to 293 K



this direction, atoms in WTe_2 do not line up in perfect atomic columns meaning that exact atomic positions cannot be assigned despite the clarity of the image.

Examining again in Fig. 4d, it is possible to assign the lattice directions a and b , as shown by the arrows. This confirms that the W zigzag or 1D chains, which form along the b crystallographic direction in T_d WTe_2 , are parallel to the long axis of the nanobelt as expected.

3.5 Electrical characterisation

EBL was used to contact individual WTe_2 nanobelts. This allowed the electrical behaviour of the crystalline nanobelts WTe_2 to be probed without the influence of junctions between WTe_2 grains. An AFM map of a device is shown in Fig. 5a, with corresponding height profile in Fig. 5b.

The two-terminal current–voltage (IV) response of a nanobelt device is shown in Fig. 5c. The device response is ohmic over the measured region. The dimensions from AFM allowed the resistivity of the device to be calculated, and this was found to be $9.3 \times 10^{-6} \Omega\cdot\text{m}$. This low resistivity is expected due to the semimetallic nature of WTe_2 . Interestingly, this resistivity matches almost exactly the values measured by Song et al. [23] in their paper on the potential use of single-crystal WTe_2 nanobelts as electrical interconnects in nanoelectronics. Their synthesis method requires the deposition of films of W and Cu that are then exposed to Te vapour. This causes a CuTe_x alloy to form, in which WTe_2 grows. Following this a post-growth etch is needed to remove residual CuTe_x [47]. The synthesis method in this work is more straight-forward and does not require a post-growth etch offering a potential advantage. The nanobelts produced here have a very similar form, which is the crystallinity and electrical response to the work of Song et al., indicating that WTe_2 is likely of a similar quality and, thus, suitable for similar applications.

The temperature dependence of the WTe_2 nanobelt resistance was investigated, with the results shown in Fig. 5d. The nanobelt shows very little change in resistivity with temperature, becoming $\sim 10\%$ less resistive as the temperature is increased from 77 to 300 K. A small change in resistivity is unsurprising for a semimetallic material, though a trend of decreasing resistivity with temperature is more usually associated with a semiconductor. There is some variation in literature reports of WTe_2 resistivity change as a function of temperature. Some works on thin crystals of WTe_2 show a reduction in resistivity with increasing temperature due to Anderson localization effects. However, that was for much thinner (3–4 layer) flakes, while the nanobelt examined here was ~ 120 layers [15, 23]. Works on thicker samples of WTe_2 generally show increasing resistivity as the temperature is increased. The magnitude of this effect is reported as being

between $\sim 5\%$ and $\sim 500\%$ change over a similar temperature window to that examined in this work [23, 31, 51, 75]. It is possible that effects such as the formation of a potential barrier at the contacts due to surface oxidation may also be influencing results seen in this and other works. Further studies would be required to fully understand the observed result.

4 Conclusion

We developed a method to synthesise large-area films of WTe_2 from pre-deposited W and Te layers. Successful conversion of these layers to WTe_2 films was confirmed with various spectroscopies. SEM showed that the polycrystalline films consisted of two different morphologies, one being regions of nanobelts up to $10 \mu\text{m}$ in length. The films were found to be stoichiometric WTe_2 but with a significant amount of surface oxidation. In line with the previous reports of WTe_2 oxidation being self-limiting, the oxide level in the bulk of the film was found to be substantially lower.

Further to this, we isolated individual nanobelts from the films to allow additional characterisation. Through TEM analysis, the nanobelts were shown to be highly crystalline with low defect densities. Combined with promising initial electrical results, this indicates the potential for these nanobelts to be used in investigations where previously mechanically exfoliated CVT crystals were used.

This ability to yield both WTe_2 films and nanobelts in a straight-forward manner at relatively low synthesis temperature is a compelling advantage of this growth method over those used in many previous studies.

Acknowledgements This work was financially supported by Science Foundation Ireland (SFI, grant numbers: 15/SIRG/3329, 12/RC/2278_P2, PL_15/IA/3131), the Irish Research Council (Project 204486, Award 13653), Science Foundation Ireland and the Royal Society Fellowship (URF/RI/191637). The SEM and (S)TEM imaging for this project was carried out at the Advanced Microscopy Laboratory (AML), Trinity College Dublin, Ireland. The AML is an SFI supported imaging and analysis centre, part of the CRANN Institute and affiliated to the AMBER centre. G.S.D and T S-L acknowledge the European Commission under the project Graphene Flagship (Grant No. 881603) and the German Ministry of Education and Research (BMBF) under ACDC (Grant No. 13N15100).

References

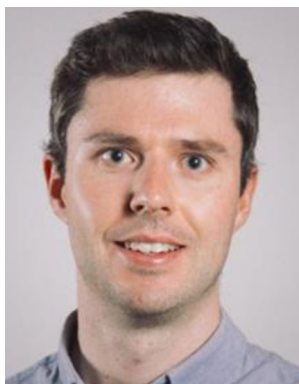
1. Gong CH, Zhang YX, Chen W, Chu JW, Lei TY, Pu JR, Dai LP, Wu CY, Cheng YH, Zhai TY, Li L, Xiong J. Electronic and optoelectronic applications based on 2D novel anisotropic transition metal dichalcogenides. *Adv Sci*. 2017;4(12):1700231.

2. Liu Y, Weiss NO, Duan XD, Cheng HC, Huang Y, Duan X. Van der Waals heterostructures and devices. *Nat Rev Mater*. 2016;1(9):16042.
3. Brown BE. The crystal structures of WTe_2 and high-temperature $MoTe_2$. *Acta Crystallogr A*. 1966;20(2):268.
4. Lu N, Zhang C, Lee CH, Oviedo JP, Nguyen MAT, Peng X, Wallace RM, Robinson JA, Wang J, Cho K, Kim MJ. Atomic and electronic structures of WTe_2 probed by high resolution electron microscopy and ab initio calculations. *J Phys Chem C*. 2016;120(15):8364.
5. Qian X, Liu J, Fu L, Li J. Quantum spin Hall effect in two-dimensional transition metal dichalcogenides. *Science*. 2014;346(6215):1344.
6. Revolinsky E, Beerntsen D. Electrical properties of the $MoTe_2$ - WTe_2 and $MoSe_2$ - WSe_2 systems. *J Appl Phys*. 1964;35(7):2086.
7. Champion JA. Some properties of (Mo, W) (Se, Te_2). *Br J Appl Phys*. 1965;16(7):1035.
8. Kabashima S. Electrical properties of Tungsten-Ditelluride WTe_2 . *J Phys Soc Jpn*. 1966;21(5):945.
9. Troadec JP, Bideau D, Guyon E. Transport properties of conducting and semiconducting anisotropic mixtures. *J Phys C: Solid State Phys*. 1981;14(32):4807.
10. Knop O, Haraldsen H. A note on the system wolfram-tellurium. *Can J Chem*. 1956;34(8):1142.
11. Goldschmidt VM. Crystal structure and chemical constitution. *Trans Faraday Soc*. 1929;25:253.
12. Torun E, Sahin H, Cahangirov S, Rubio A, Peeters FM. Anisotropic electronic, mechanical, and optical properties of monolayer WTe_2 . *J Appl Phys*. 2016;119(7):074307.
13. Kim Y, Jhon YI, Park J, Kim JH, Lee S, Jhon YM. Anomalous Raman scattering and lattice dynamics in mono- and few-layer WTe_2 . *Nanoscale*. 2016;8(4):2309.
14. Ali MN, Xiong Y, Flynn S, Tao J, Gibson QD, Schoop LM, Liang T, Haldolaarachchige N, Hirschberger M, Ong NP, Cava RJ. Large, non-saturating magnetoresistance in WTe_2 . *Nature*. 2014;514(7521):205.
15. Wang L, Gutiérrez-Lezama I, Barreteau C, Ubrig N, Giannini E, Morpurgo AF. Tuning magnetotransport in a compensated semimetal at the atomic scale. *Nat Commun*. 2015;6(1):8892.
16. Wang Y, Wang L, Liu X, Wu H, Wang P, Yan D, Cheng B, Shi Y, Watanabe K, Taniguchi T, Liang SJ, Miao F. Direct evidence for charge compensation-induced large magnetoresistance in thin WTe_2 . *Nano Lett*. 2019;19(6):3969.
17. Fei Z, Zhao W, Palomaki TA, Sun B, Miller MK, Zhao Z, Yan J, Xu X, Cobden DH. Ferroelectric switching of a two-dimensional metal. *Nature*. 2018;560(7718):336.
18. Fatemi V, Wu S, Cao Y, Bretheau L, Gibson QD, Watanabe K, Taniguchi T, Cava RJ, Jarillo-Herrero P. Electrically tunable low-density superconductivity in a monolayer topological insulator. *Science*. 2018;362(6417):926.
19. Kang D, Zhou Y, Yi W, Yang C, Guo J, Shi Y, Zhang S, Wang Z, Zhang C, Jiang S, Li A, Yang K, Wu Q, Zhang G, Sun L, Zhao Z. Superconductivity emerging from a suppressed large magnetoresistant state in tungsten ditelluride. *Nat Commun*. 2015;6(1):7804.
20. Soluyanov AA, Gresch D, Wang Z, Wu Q, Troyer M, Dai X, Bernevig BA. Type-II Weyl semimetals. *Nature*. 2015;527(7579):495.
21. Li P, Wen Y, He X, Zhang Q, Xia C, Yu ZM, Yang SA, Zhu Z, Alshareef HN, Zhang XX. Evidence for topological type-II Weyl semimetal WTe_2 . *Nat Commun*. 2017;8(1):2150.
22. Zhang W, Wu Q, Zhang L, Cheong SW, Soluyanov AA, Wu W. Quasiparticle interference of surface states in the type-II Weyl semimetal WTe_2 . *Phys Rev B*. 2017;96(16):165125.
23. Song S, Kim SY, Kwak J, Jo Y, Kim JH, Lee JH, Le JU, Kim JU, Yun HD, Sim Y, Wang J, Lee DH, Seok AH, Kim TI, Cheong H, Lee Z, Kwon SY. Electrically Robust Single-Crystalline WTe_2 Nanobelts for Nanoscale Electrical Interconnects. *Adv Sci*. 2019;6(3):1801370.
24. Li J, Hong M, Sun L, Zhang W, Shu H, Chang H. Enhanced electrocatalytic hydrogen evolution from large-scale, facile-prepared, highly crystalline WTe_2 nanoribbons with weyl semimetallic phase. *ACS Appl Mater Interfaces*. 2018;10(1):458.
25. Srinivaas M, Wu CY, Duh JG, Hu YC, Wu JM. Multi-walled carbon-nanotube-decorated tungsten ditelluride nanostars as anode material for lithium-ion batteries. *Nanotechnology*. 2019;31(3):035406.
26. Hong M, Li J, Zhang W, Liu S, Chang H. Semimetallic 1T' WTe_2 nanorods as anode material for the sodium ion battery. *Energy Fuels*. 2018;32(5):6371.
27. Gholamvand Z, McAteer D, Backes C, McEvoy N, Harvey A, Berner NC, Hanlon D, Bradley C, Godwin I, Rovetta A, Lyons MEG, Duesberg GS, Coleman JN. Comparison of liquid exfoliated transition metal dichalcogenides reveals $MoSe_2$ to be the most effective hydrogen evolution catalyst. *Nanoscale*. 2016;8(10):5737.
28. Zhou Y, Silva JL, Woods JM, Pondick JV, Feng Q, Liang Z, Liu W, Lin L, Deng B, Brena B, Xia F, Peng H, Liu Z, Wang H, Araujo CM, Cha JJ. Revealing the contribution of individual factors to hydrogen evolution reaction catalytic activity. *Adv Mater*. 2018;30(18):1706076.
29. Kwon H, Ji B, Bae D, Lee JH, Park HJ, Kim DH, Kim YM, Son YW, Yang H, Cho S. Role of anionic vacancy for active hydrogen evolution in WTe_2 . *Appl Surf Sci*. 2020;515:145972.
30. Zhou Y, Pondick JV, Silva JL, Woods JM, Hynek DJ, Matthews G, Shen X, Feng Q, Liu W, Lu Z, Liang Z, Brena B, Cai Z, Wu M, Jiao L, Hu S, Wang H, Araujo CM, Cha JJ. Unveiling the interfacial effects for enhanced hydrogen evolution reaction on MoS_2/WTe_2 hybrid structures. *Small*. 2019;15(19):1900078.
31. Lee CH, Silva EC, Calderin L, Nguyen MAT, Hollander MJ, Bersch B, Mallouk TE, Robinson JA. Tungsten Ditelluride: a layered semimetal. *Sci Rep*. 2015;5(1):10013.
32. Zhao Y, Liu H, Yan J, An W, Liu J, Zhang X, Wang H, Liu Y, Jiang H, Li Q, Wang Y, Li XZ, Mandrus D, Xie XC, Pan M, Wang J. Anisotropic magnetotransport and exotic longitudinal linear magnetoresistance in WTe_2 crystals. *Phys Rev B*. 2015;92(4):041104.
33. Bi R, Feng Z, Li X, Zhao J, Fan J, Shi Y, Yu D, Wu X. Quantum oscillations of thermopower in WTe_2 thin films. *Phys Rev B*. 2019;100(23):235405.
34. Chen K, Chen Z, Wan X, Zheng Z, Xie F, Chen W, Gui X, Chen H, Xie W, Xu J. A simple method for synthesis of high-quality millimeter-scale 1T' transition-metal telluride and near-field nanooptical properties. *Adv Mater*. 2017;29(38):1700704.
35. Naylor CH, Parkin WM, Gao Z, Kang H, Noyan M, Wexler RB, Tan LZ, Kim Y, Kehayias CE, Streller F, Zhou YR, Carpick R, Luo Z, Park YW, Rappe AM, Drndić M, Kikkawa JM, Johnson ATC. Large-area synthesis of high-quality monolayer 1T'- WTe_2 flakes. *2D Materials*. 2017;4(2):021008.
36. Pan XC, Chen X, Liu H, Feng Y, Wei Z, Zhou Y, Chi Z, Pi L, Yen F, Song F, Wan X, Yang Z, Wang B, Wang G, Zhang Y. Pressure-driven dome-shaped superconductivity and electronic structural evolution in tungsten ditelluride. *Nat Commun*. 2015;6(1):7805.
37. Gong JX, Yang J, Ge M, Wang YJ, Liang DD, Luo L, Yan X, Zhen WL, Weng SR, Pi L, Zhang CJ, Zhu WK. Non-stoichiometry

- effects on the extreme magnetoresistance in weyl semimetal WTe_2 . *Chin Phys Lett*. 2018;35(9):097101.
38. Lu W, Zhang Y, Zhu Z, Lai J, Zhao C, Liu X, Liu J, Sun D. Thin tungsten telluride layer preparation by thermal annealing. *Nanotechnology*. 2016;27(41):414006.
 39. Woods JM, Shen J, Kumaravadivel P, Pang Y, Xie Y, Pan GA, Li M, Altman EI, Lu L, Cha JJ. Suppression of magnetoresistance in thin WTe_2 flakes by surface oxidation. *ACS Appl Mater Interfaces*. 2017;9(27):23175.
 40. Zhou J, Liu F, Lin J, Huang X, Xia J, Zhang B, Zeng Q, Wang H, Zhu C, Niu L, Wang X, Fu W, Yu P, Chang TR, Hsu CH, Wu D, Jeng HT, Huang Y, Lin H, Shen Z, Yang C, Lu L, Suenaga K, Zhou W, Pantelides ST, Liu G, Liu Z. Large-area and high-quality 2D transition metal telluride. *Adv Mater*. 2017;29(3):1603471.
 41. Li J, Cheng S, Liu Z, Zhang W, Chang H. Centimeter-scale, large-area, few-layer 1T'- WTe_2 films by chemical vapor deposition and its long-term stability in ambient condition. *J Phys Chem C*. 2018;122(12):7005.
 42. Lee CS, Oh SJ, Heo H, Seo SY, Kim J, Kim YH, Kim D, Okello OFN, Shin H, Sun JH, Choi SY, Kim JS, Kim JK, Jo MH. Epitaxial van der Waals contacts between transition-metal dichalcogenide monolayer polymorphs. *Nano Lett*. 2019;19(3):1814.
 43. de Melo O, Sánchez M, Borroto A, de Melo C, García BJ, Pau JL, Horwat D. WTe_2 synthesis by tellurization of W precursors using isothermal close space vapor transport annealing. *Physica Status Solid(A)* 2018;215(23):1800425.
 44. Woods JM, Hynek D, Liu P, Li M, Cha JJ. Synthesis of WTe_2 nanowires with increased electron scattering. *ACS Nano*. 2019;13(6):6455.
 45. Song S, Sim Y, Kim SY, Kim JH, Oh I, Na W, Lee DH, Wang J, Yan S, Liu Y, Kwak J, Chen JH, Cheong H, Yoo JW, Lee Z, Kwon SY. Wafer-scale production of patterned transition metal ditelluride layers for two-dimensional metal-semiconductor contacts at the Schottky-Mott limit. *Nat Electron*. 2020;3(4):207.
 46. Zhou Y, Jang H, Woods JM, Xie Y, Kumaravadivel P, Pan GA, Liu J, Liu Y, Cahill DG, Cha JJ. Direct synthesis of large-scale WTe_2 thin films with low thermal conductivity. *Adv Funct Mater*. 2017;27(8):1605928.
 47. Kwak J, Jo Y, Song S, Kim JH, Kim SY, Lee JU, Lee S, Park J, Kim K, Lee GD, Yoo JW, Kim SY, Kong YM, Lee GH, Lee WG, Park J, Xu X, Cheong H, Yoon E, Lee Z, Kwon SY. Single-crystalline nanobelts composed of transition metal ditellurides. *Adv Mater*. 2018;30(30):1707260.
 48. Walsh LA, Yue R, Wang Q, Barton AT, Addou R, Smyth CM, Zhu H, Kim J, Colombo L, Kim MJ, Wallace RM, Hinkle CL. WTe_2 thin films grown by beam-interrupted molecular beam epitaxy. *2D Materials*. 2017;4(2):025044.
 49. Zhu X, Li S, Li J, Ali RN, Naz H, Liu P, Feng C, Xiang B. Free-standing WTe_2 QD-doped NiSe/C nanowires for highly reversible lithium storage. *Electrochim Acta*. 2019;295:22.
 50. Vermeulen PA, Momand J, Kooi BJ. Low temperature epitaxy of tungsten-telluride heterostructure films. *CrystEngComm*. 2019;21(22):3409.
 51. Chen Y, Chen Y, Ning J, Chen L, Zhuang W, He L, Zhang R, Xu Y, Wang X. Observation of Shubnikov-de Haas oscillations in large-scale Weyl semimetal WTe_2 films. *Chin Phys Lett*. 2020;37(1):017104.
 52. Sun Y, Fujisawa K, Terrones M, Schaak RE. Solution synthesis of few-layer WTe_2 and $\text{Mo}_x\text{W}_{1-x}\text{Te}_2$ nanostructures. *J Mater Chem C*. 2017;5(43):11317.
 53. Giri A, Yang H, Jang W, Kwak J, Thiyagarajan K, Pal M, Lee D, Singh R, Kim C, Cho K, Soon A, Jeong U. Synthesis of atomically thin transition metal ditelluride films by rapid chemical transformation in solution phase. *Chem Mater*. 2018;30(7):2463.
 54. Duffy R, Foley P, Filippone B, Mirabelli G, O'Connell D, Sheehan B, Carolan P, Schmidt M, Cherkaoui, Gatensby R, Hallam T, Duesberg G, Crupi F, Nagle R, Hurley PK. Structural and electrical investigation of MoS_2 thin films formed by thermal assisted conversion of Mo metal. *ECS J Solid State Sci Technol* 2016;5(11):Q3016.
 55. Richoux V, Diliberto S, Boulanger C, Lecuire JM. Pulsed electrodeposition of bismuth telluride films: influence of pulse parameters over nucleation and morphology. *Electrochim Acta*. 2007;52(9):3053.
 56. Mc Manus JB, Cunningham G, McEvoy N, Cullen CP, Gity F, Schmidt M, McAteer D, Mullarkey D, Shvets IV, Hurley PK, Hallam T, Duesberg GS. Growth of 1T' MoTe_2 by thermally assisted conversion of electrodeposited tellurium films. *ACS Appl Energy Mater*. 2019;2(1):521.
 57. McEvoy N, Peltekis N, Kumar S, Rezvani E, Nolan H, Keeley GP, Blau WJ, Duesberg GS. Synthesis and analysis of thin conducting pyrolytic carbon films. *Carbon*. 2012;50(3):1216.
 58. Jones L, Yang H, Pennycook TJ, Marshall MSJ, Van Aert S, Browning ND, Castell MR, Nellist PD. Smart align—a new tool for robust non-rigid registration of scanning microscope data. *Adv Struct Chem Imaging*. 2015;1(1):8.
 59. Wenner S, Jones L, Marioara CD, Holmestad R. Atomic-resolution chemical mapping of ordered precipitates in Al alloys using energy-dispersive X-ray spectroscopy. *Micron*. 2017;96:103.
 60. Zhou L, Xu K, Zubair A, Zhang X, Ouyang F, Palacios T, Dresselhaus MS, Li Y, Kong J. Role of molecular sieves in the CVD synthesis of large-area 2D MoTe_2 . *Adv Funct Mater*. 2017;27(3):1603491.
 61. Mc Manus JB, Horvath DV, Browne MP, Cullen CP, Cunningham G, Hallam T, Zhussupbekov K, Mullarkey D, Ó Coileáin C, Shvets IV, Pumera M, Duesberg GS, McEvoy N. Low-temperature synthesis and electrocatalytic application of large-area PtTe_2 thin films. *Nanotechnology*. 2020;31(37):375601.
 62. Cao Y, Sheremetyeva N, Liang L, Yuan H, Zhong T, Meunier V, Pan M. Anomalous vibrational modes in few layer WTe_2 revealed by polarized Raman scattering and first-principles calculations. *2D Materials*. 2017;4(3):035024.
 63. Jiang YC, Gao J, Wang L. Raman fingerprint for semi-metal WTe_2 evolving from bulk to monolayer. *Sci Rep*. 2016;6(1):19624.
 64. Ma H, Chen P, Li B, Li J, Ai R, Zhang Z, Sun G, Yao K, Lin Z, Zhao B, Wu R, Tang X, Duan X, Duan X. Thickness-tunable synthesis of ultrathin type-II dirac semimetal PtTe_2 single crystals and their thickness-dependent electronic properties. *Nano Lett*. 2018;18(6):3523.
 65. Ma X, Guo P, Yi C, Yu Q, Zhang A, Ji J, Tian Y, Jin F, Wang Y, Liu K, Xia T, Shi Y, Zhang Q. Raman scattering in the transition-metal dichalcogenides of 1T' MoTe_2 , T_d MoTe_2 and T_d WTe_2 . *Phys Rev B*. 2016;94(21):214105.
 66. Ye F, Lee J, Hu J, Mao Z, Wei J, Feng PXL. Environmental instability and degradation of single- and few-layer WTe_2 nanosheets in ambient conditions. *Small*. 2016;12(42):5802.
 67. Hou F, Zhang D, Sharma P, Singh S, Wu T, Seidel J. Oxidation kinetics of WTe_2 surfaces in different environments. *ACS Appl Electron Mater*. 2020;2(7):2196.
 68. Shawkat MS, Gil J, Han SS, Ko TJ, Wang M, Dev D, Kwon J, Lee GH, Oh KH, Chung HS, Roy T, Jung YJ, Jung Y. Thickness-independent semiconducting-to-metallic conversion in wafer-scale two-dimensional PtSe_2 layers by plasma-driven chalcogen defect engineering. *ACS Appl Mater Interfaces*. 2020;12(12):14341.
 69. Her YC, Huang SL. Growth mechanism of Te nanotubes by a direct vapor phase process and their room-temperature CO and NO_2 sensing properties. *Nanotechnology*. 2013;24(21):215603.
 70. Predel B. *Phase Equilibria, Crystallographic and Thermodynamic Data of Binary Alloys*. Heidelberg: Springer; 1998.

71. Callanan JE, Hope GA, Weir RD, Westrum EF. Thermodynamic properties of tungsten ditelluride (WTe_2) I. The preparation and lowtemperature heat capacity at temperatures from 6 K to 326 K. *J Chem Thermodyn* 1992;24(6):627.
72. Srivastava SK, Avasthi BN. Layer type tungsten dichalcogenide compounds: their preparation, structure, properties and uses. *J Mater Sci*. 1985;20(11):3801.
73. Jones L, Nellist PD. Identifying and correcting scan noise and drift in the scanning transmission electron microscope. *Microsc Microanal*. 2013;19(4):1050.
74. Jones L. Quantitative ADF-STEM: acquisition, analysis and interpretation. *IOP Conf Ser Mater Sci Eng*. 2016;109:012008.
75. Jha R, Onishi S, Higashinaka R, Matsuda TD, Ribeiro RA, Aoki Y. Anisotropy in the electronic transport properties of Weyl semimetal WTe_2 single crystals. *AIP Adv*. 2018;8(10):101332.

Publisher's Note Springer Nature remains neutral with regard to jurisdictional claims in published maps and institutional affiliations.



Dr. John McManus received a Ph.D. degree in chemistry from Trinity College Dublin (TCD), Dublin, Ireland, in 2019. He received a B.A. (Mod.) degree in physics and chemistry of advanced materials from TCD in 2013 and was awarded a gold medal and the Henderson-Lloyd prize. He now works as a post-doctoral researcher in AMBER & the School of Chemistry, TCD. His research interests include the synthesis of two

dimensional (2D) materials, and the fabrication of electrical devices based on 2D materials.



Dr. Niall McEvoy received a Ph.D. degree in physics from Trinity College Dublin (TCD), Dublin, Ireland, in 2011. Following the completion of several industry-focused postdoctoral appointments, he now works as a Science Foundation Ireland (SFI) funded Principal Investigator in AMBER & the School of Chemistry, TCD. There he leads the Architecture and Synthesis of Integrated Nanostructures (ASIN) research group. His research interests include scalable synthesis of nanomaterials

and subsequent assessment of their viability for use in diverse application areas ranging from (opto) electronics to electrocatalysis. To date, he has co-authored ~130 peer-reviewed journal papers which have been cited >8000 times.